Self-organization of inorganic nanocrystals

Self-organization of inorganic nanocrystals

M P Pileni

Laboratoire LM2N, Université P et M Curie (Paris VI), BP 52, 4 Place Jussieu, F-75231 Paris Cedex 05, France

Abstract
Self-organizations of inorganic nanocrystals in 1D, 2D and 3D superlattices are described. In the latter case, supra-crystals with face-centred-cubic (fcc) structure are demonstrated. Collective properties due to the nanocrystal organization are described. These properties are either intrinsic or due to dipolar interactions.

(Some figures in this article are in colour only in the electronic version)

1. Introduction

Spherical objects like oranges or balls having the same diameter self-organize in compact hexagonal networks. Crystals are usually atomic in origin, such as the regular periodic arrangement of silicon and oxygen atoms in quartz. Nanocrystals having a low size distribution are able to self-organize either in 2D or 3D superlattices. In the latter case, the crystals formed by a periodic arrangement are called supra-crystals [1–17]. They are a new and challenging area in nanotechnology [18, 19].

In the last few years it has been well demonstrated [1] that, due to dipolar interactions, collective optical [1, 20–25], magnetic [1, 26–31] and transport [1, 32, 33] properties result from the ordered periodic arrangement of nanocrystals in 2D superlattices.

We discovered that self-organization of nanocrystals in fcc supra-crystals induces intrinsic collective properties. Hence, a mechanical role in the control of cobalt nanocrystals organization in columns is observed [34, 35]. There is an intrinsic dynamic behaviour (lattice vibrations) that is absent in non-crystalline solids composed of nanoparticles [36–38]. These coherences could explain the change in the transport properties observed previously with silver nanocrystal self-organizations [33].

In this paper the review is organized as follows. We first describe the way to produce nanocrystals. Self-organization of organic molecules as surfactants permit one to produce water in oil reverse micelles used as nanoreactor to produce inorganic nanocrystals (section 2). When the size of nanocrystals is highly controlled they self-organize in 2D and 3D superlattices. In section 3 we describe how to control the organization of these inorganic nanocrystals. We demonstrate that the deposition mode permits one to produce with the same nanocrystals either
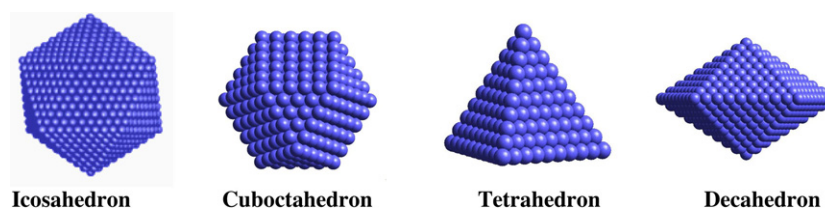
Figure 1. Representation of the stable precursor nuclei for the formation of copper nanocrystals.

amorphous aggregates or supra-crystals organized in an fcc structure. Van der Waals, sterical, capillary, and dipolar forces control the various self-organization. In section 4 we demonstrate vibrational coherence between nanocrystals when they are self-organized in fcc supra-crystals. Then we demonstrate other collective optical and magnetic properties mainly due to dipolar interactions. Note that the magnetic properties markedly depend on the structure of the self-organization of inorganic nanocrystals.

2. Synthesis of nanocrystals via reverse micelles

Reverse micelles are water-in-oil droplets stabilized by a surfactant [39]. These droplets are displaced randomly and subjected to Brownian motion. They exchange their water contents and reform two distinct micelles. Furthermore, the size of the water-in-oil droplets linearly increases, i.e., the micellar concentration decreases, with increasing the water content, defined as $w = [H_2O]\backslash[AOT]$ where AOT is 2 bis (2-ethylhexyl)sulfosuccinate. Let us consider two reactants A (such as copper ions) and B (hydrazine) solubilized in two distinct micellar solutions. On mixing them, and because of the exchange process, A and B are in contact and react. It is thus possible to induce a very wide range of chemical reactions. At fixed surfactant and reactant concentration, the number of reactants per micelle increases, following a Poisson distribution. On increasing w, the water structure inside the droplet evolves from a morphology similar to ice to that of free water and consequently the solvation of the counter ions inside the droplet increases [40]. This induces a change in the chemical reaction yield (i.e., redox potential, solubility, etc). Above $w = 10$, the counter ions of the surfactant are hydrated and 'free' bulk water appears in the droplets [41].

Reverse micelles have been used for almost 17 years to produce a very wide range of nanocrystals such as II–VI semiconductors and metals [42, 43]. With silver and copper nanocrystals, no traces of oxide are detected. This is mainly attributed to the fact that a functionalized surfactant (i.e., the head polar group of the surfactant is one of the reactants) is used to produce the nanocrystals [44]. At a fixed reactant concentration, the increase in the water content induces an increase in the number of reactants per micelle and in the amount of solvated reactant ions.

We know from crystal growth studies that the origin of the material structure is related to the constituent nuclei. Bulk silver and copper metal materials have fcc structures and their nuclei are icosahedral, decahedral, cubooctahedral and tetrahedral [45] (figure 1). The transmission electron microscopy (TEM) images of copper nanocrystals, obtained at the end of the synthesis (5 h) vary with w [46, 47]. Below $w = 10$, the average particle size increases with w but at $w > 10$ the particle size remains the same. This is explained by the increase in the number of reactants per micelle, i.e., the number of nuclei per micelle, favouring an increase in the particle size. At $w = 3$, most of the entities are spherical copper
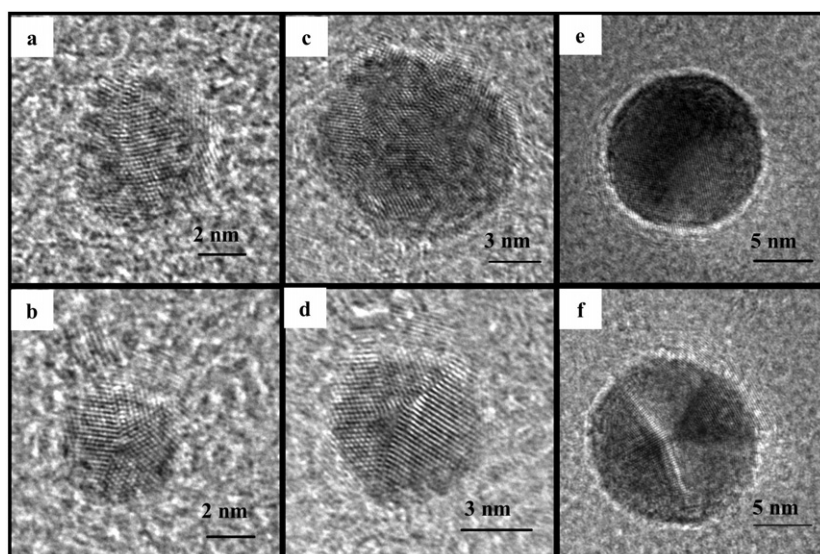
Figure 2. HRTEM images of spherical ((a), (c) and (e)) and decahedral ((b), (d), (f)) copper nanocrystals synthesized in $Cu(AOT)_2$/NaAOT, water, and isooctane reverse micelles at various water contents. [AOT] = 0.1 M; $[Cu(AOT)_2] = 10^{-2}$ M. ((a), (b)) $w = 3$; ((c), (d)) $w = 5$; ((e), (f)) $w = 10$.

particles either made of fcc clusters (figure 2(a)) or characterized by a more or less regular decahedral structure (figure 2(b)). On increasing w to 5, similar crystalline structures are produced (figures 2(c) and (d)). A further increase in w to 10 favours the increase in the number of nanocrystals characterized by a regular fcc structure attributed to cubooctahedra (figure 2(e)). These structures coexist with regular decahedra (figure 2(f)). Hence, both nanoparticle crystallinity and size increase with w (figure 2). A structural study [47] shows that monocrystal spheres and the regular decahedra result from the growth of cubooctahedral and decahedral nuclei [48], respectively. Hence, their shapes are closely related to that of the corresponding nuclei. The homogeneous growth of cubooctahedral nuclei makes possible the formation of spherical nanocrystals. Similarly, regular decahedra, formed by five deformed tetrahedral subunits twinned by their {111} planes and characterized by a five-fold symmetry, are obtained (figure 2(f)). The formation of such unusual structures results from the simultaneous and regular growth of the ten enclosed {111} facets. No transformation such as facet truncation or preferential growth of facets occurs during the growth process. This confirms that AOT surfactant molecules forming reverse micelles do not play a role in such growths. It must be noted that the produced decahedra have an average size of 10–15 nm. Similar behaviour was obtained for silver nanocrystals with coexisting icosahedral and decahedral nanocrystals [49]. Because it is possible to produce large nanocrystals having the same geometry as their nuclei, it is concluded that there is homogeneous growth of nuclei inside the reverse micelles. This is probably a proof that the mechanism of crystal growth is the same at various scales. Furthermore, it proves that the control of the shape is mainly due to specific adsorption of elements on nanocrystal surfaces. Their amounts can be very small and considered as impurities. This also explains why, when free surfactant molecules are present in the solution during the synthesis, the control of the nanocrystal shape is not highly reproducible [50].
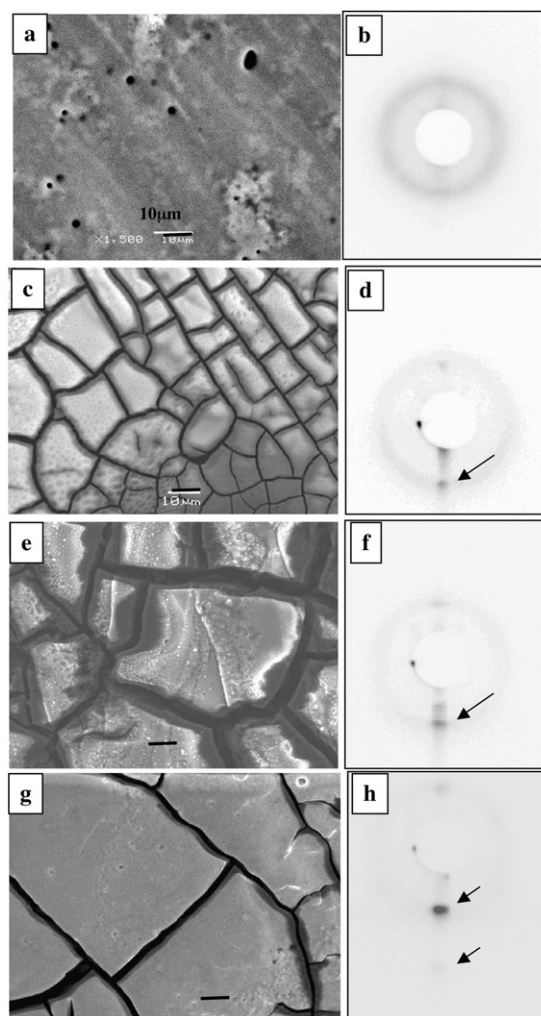
Figure 3. SEM patterns obtained by deposition of cobalt nanocrystals on highly oriented pyrolytic graphite substrate. The different substrate temperatures and corresponding x-ray diffraction patterns are ((a), (b)) $T = 10\,°C$, ((c), (d)) $T = 25\,°C$, ((e), (f)) $T = 35\,°C$, ((g), (h)) $T = 45\,°C$.

## 3. Self-organization in 2D and 3D superlattices

Self-organization of nanocrystals in compact hexagonal networks is governed by the control of the particle size, and the particle–particle and particle–substrate interactions, whereas other structures such as rings and fingers are governed by Marangoni instabilities [1]. To determine the influence of nanocrystal ordering on the supra-crystals properties, it is important to produce simultaneously ordered and disordered aggregates. The ordering is tuned by changing the substrate temperature during the deposition process of nanocrystals [14–17]. At low temperatures, the deposition gives rise to the formation of a non-homogeneous thin film coexisting with aggregates (figure 3(a)). The x-ray diffraction pattern (figure 3(b)) reveals a broad diffuse ring attributed to an amorphous material. On increasing the temperature ($18\,°C < T < 45\,°C$), the film morphology drastically changes (figures 3(c), (e), (g)).
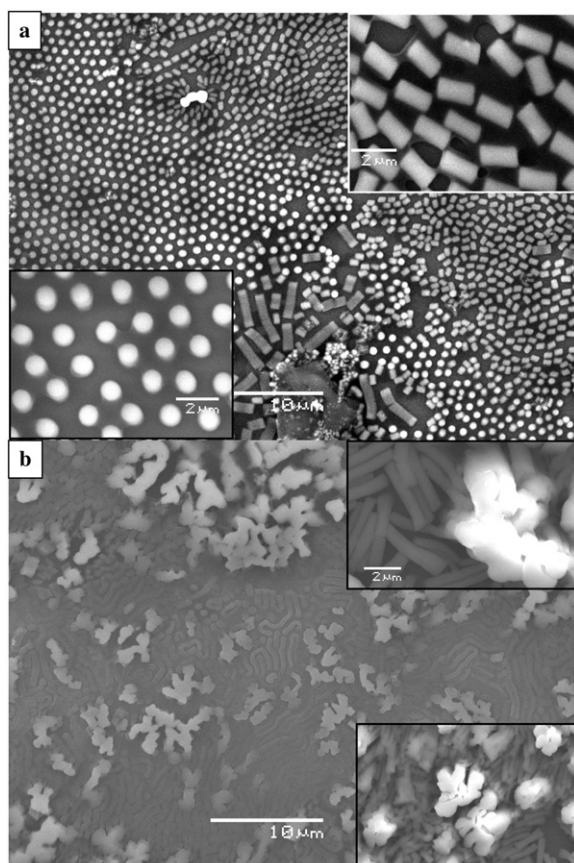
Figure 4. Scanning electron microscopy patterns of mesostructures of 5.7 nm cobalt nanocrystals having 13% (a) and 18% (b) size distributions.

Isolated domains like pavements with a rather smooth surface are observed. On increasing the substrate temperature the pavement area increases. The x-ray diffraction patterns (figures 3(d), (f), (h)) clearly show the high degree of ordering of the nanocrystals with fcc supra-crystal formation [16, 17]. Thus it is definitely possible to tune the nanocrystal ordering from amorphous aggregates to fcc supra-crystals. Such behaviour seems to be valid for a large class of materials as soon as the nanocrystal size distribution is low enough and the particle–particle attraction is not too strong.

Supra-crystals forming columns [34, 35] are produced by applying a magnetic field perpendicular to the highly oriented pyrolytic graphite (HOPG) substrate during the evaporation process of a colloidal solution containing cobalt nanocrystals. Figure 4(a) shows a well-defined and highly compact structure with columns and/or dots and very few labyrinths of cobalt nanocrystals having a very low size distribution. Under such experimental conditions, it is demonstrated that the columns of nanocrystals form a supra-crystal ordered in a fcc structure. On increasing the nanocrystal size distribution, keeping a similar average diameter, the scanning electron microscopy (SEM) images markedly change with formation of a large number of flower-like and labyrinthine patterns (figure 4(b)). Magnification of these structures shows coalescence of either upright or fallen columns forming worm-like or labyrinthine structures (insets figure 4(b)). From experiments and theoretical models a mechanism of
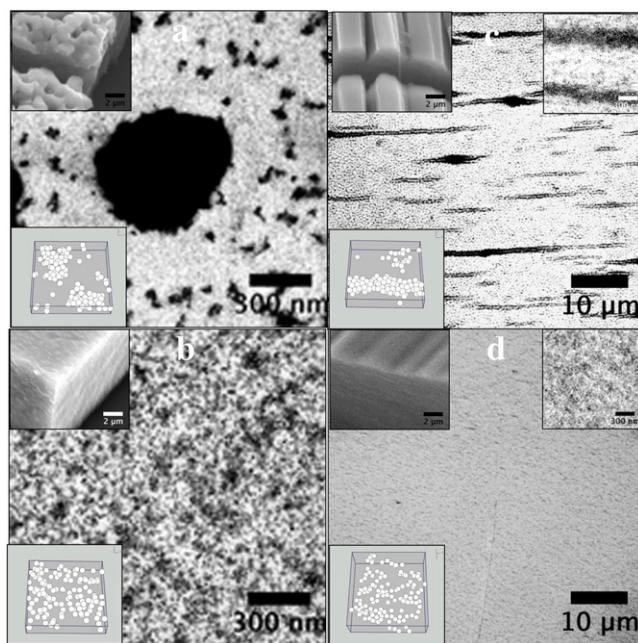
Figure 5. TEM patterns obtained with C8 ((a), (c)) and C12 ((b), (d)) subjected ((c), (d)) or not ((a), (b)) to a magnetic field. The insets correspond to higher magnification, simulation and to assemblies made at high nanocrystal concentrations.

patterns formation in a perpendicular applied field is proposed: during the evaporation process, a liquid–gas phase transition [51] occurs with formation of a concentrated solution of nanocrystals in equilibrium with a diluted one. In the concentrated phase, columns (dots) are progressively formed and they tend to migrate to self-organize in hexagonal patterns. Each column is made of cobalt nanocrystals. Whatever the nanocrystal size distribution, the mechanism described above remains valid. However, when the size distribution is low enough, the nanocrystals dispersed in solution tend to diffuse and self-assemble in fcc supra-crystals with the formation of well-defined and compact columns. On increasing the nanocrystal size distribution, the interactions between particles markedly decrease and the columns are formed with disordered entities. This creates defects and the cohesive forces between columns are not large enough to keep them ordered. Columns having more or less the same sizes tend to self-assemble via van der Waals interactions forming worm-like and labyrinthine structures. This explains the change in the height of the labyrinths. The patterns show fallen columns, called cylinders above, because of the waves induced by capillary forces during the evaporation time. From this it is clear that there is a change in the mesoscopic patterns from columns ordered in fcc supra-crystals to labyrinths. To our knowledge, this is the first example of a mechanical property of supra-crystals.

The interaction between maghemite, σ-Fe$_2$O$_3$, nanocrystals is tuned by changing the coating molecules length [52, 53]. A substrate (TEM grid or cleaved graphite) is deposited in the bottom of the beaker containing the solution of nanocrystals coated either by octanoic (C$_7$H$_{15}$COOH) or dodecanoic acid (C$_{11}$H$_{23}$COOH), denoted by C8 and C12, respectively, and dispersed in cyclohexane. At the end of the evaporation, the substrate is imaged either by TEM or SEM. With no applied magnetic field, spherical aggregates with various sizes appear with C8 (figure 5(a)). In contrast, the C12-nanocrystals are randomly deposited on the TEM grid

(figure 5(b)). In a magnetic field, nanocrystals coated with C8 nanocrystals form thick striped structures in the direction of the applied field (figure 5(c)). Conversely, with C12, the TEM patterns do not show any nanocrystal organization (figure 5(d)). Similar behaviour is observed on increasing the nanocrystal concentration: with C8 nanocrystals, with no magnetic field, a very rough thick film of highly compact spherical aggregates (inset figure 5(a)) is formed whereas superimposed tubes are produced in a field (inset figure 5(b)). Conversely, with C12, a thin film is observed with (inset figure 5(d)) and without (inset figure 5(c)) an applied field. Because nanocrystals are characterized by the same magnetic dipolar moments, the changes in the organization with the coating shown in figure 5 cannot be directly attributed to the magnetic properties of the σ-Fe$_2$O$_3$ nanocrystals. Dynamic Brownian simulation takes into account the inter-particle interaction, defined as a sum of the steric repulsion due to the coating molecules, the dipole–dipole potential and the van der Waals attraction. The large variation in the energy of the most stable head–tail configuration with the particle distance is mainly due to the marked sensitivity of the van der Waals potential to the inter-particle distance. In spite of a low dipole interaction with respect to the thermal energy, there is formation of striped structures with C8-nanocrystals in a magnetic field (figure 5(c)). To explain this, both van der Waals attraction and magnetic dipoles have to be taken into account: when the coating molecules are small enough the formation of large aggregates of nanocrystals, due to the van der Waals forces, considerably enhances the long-range dipolar forces compared to isolated particles with creation of a 'macro dipolar moment' leading to an anisotropic organization of the nanoparticles (inset in figure 5(c)). On increasing the distance, no aggregation of the particles is observed even during the evaporation when particles are subjected (inset in figure 5(d)) or not (inset in figure 5(c)) to an applied magnetic field during the evaporation process. There is rather good agreement between the structures obtained from experiments and those obtained from simulations.

4. Collective properties due to self-organization

4.1. Intrinsic properties

When the incident light energy is in resonance with that of the electronic dipolar plasmon [54], scattering by cluster vibrations is observed. For spherical nanocrystals with sizes larger than ~1 nm, the cluster vibrations are described by modelling the nanocrystal with a continuum nanosphere of a diameter D equal to the size of the nanocrystal [55], and using the longitudinal, v_l, and transversal, v_t, sound velocities of bulk Ag. The vibrations are characterized by the quantum numbers n and l, and the vibrational frequencies are given by the following equation [56]:

$$v = \frac{S_{ln} v_t}{D} \tag{1}$$

where S_{ln} depends on the ratio v_l/v_t. From experimentally verified group theory rules [57], only spherical ($l = 0$) and quadrupolar ($l = 2$) modes are observed by low-frequency Raman scattering. This was confirmed from experiments and theoretical considerations [58]. While the latter modes are easily detected due to their coupling with the dipolar plasmon, the observation of the spherical modes requires a narrow size distribution of the nanocrystals [49, 59, 60]. The solid line in figure 6(a) shows the Stokes–anti-Stokes Raman spectrum of amorphous aggregates (full line). As observed previously [55] with similar systems, the quadrupolar modes appear as sharp intense lines. Figure 7 compares the Stokes lineshape of amorphous aggregates of 5 nm silver nanocrystals with the inverse size distribution $F(D^{-1})$. From equation (1), good matching of the two curves is obtained with an average sound velocity $V_t = 1500$ m s^{-1},
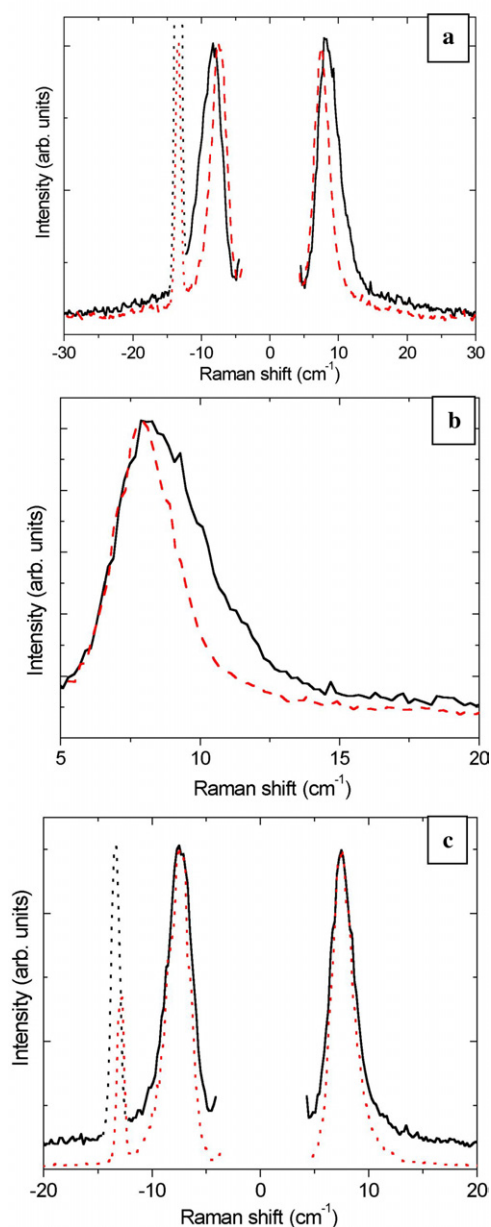
Figure 6. (a) Raman scattering spectra of 5 nm silver nanocrystals forming either amorphous aggregates (full line) or a supra-crystal (dotted line). (b) Superposition of Stokes lineshapes after horizontal shifting of amorphous aggregates and the supra-crystal. (c) Comparison of the Raman scattered intensity $I^{(3)}(\nu)$ from silver nanocrystals forming small supra-crystals with the profile $[I^{(1)}(\nu)]^2$ from amorphous aggregates of silver nanocrystals.

taking $S_{ln} = 0.83$, the theoretical value which corresponds to the V_l/V_t ratio of silver. Note that this sound speed value is close to that in bulk silver (1660 m s^{-1}). According to previous findings [59], the relatively good agreement between the inverse size histogram and the Raman
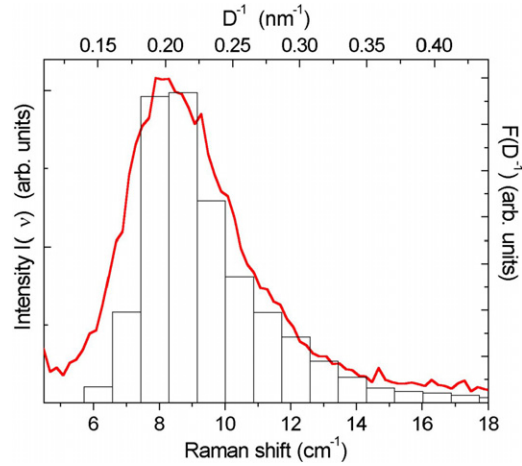
Figure 7. Comparison of the Stokes lineshapes of amorphous aggregates.

lineshape demonstrates the *intra*-nanoparticle coherence, i.e., nanocrystallinity and not *inter*-nanocrystal coherence (or supra-crystallinity). For an isolated particle, the intensity of Raman scattering by a particle vibration changes with the degree of spatial coherence, or crystallinity, inside the Ag nanocrystals. This intensity, $I^{(1)}(\nu)$, for total *intra*-nanocrystal coherence (i.e., good nanocrystal crystallinity), without *inter*-nanocrystal coherence, is given by the following expression for Stokes Raman scattering [60]:

$$I^{(1)}(\alpha) = \frac{n(\alpha) + 1}{\alpha}[\alpha^{(1)}\alpha(\alpha)]F(\alpha) \tag{2}$$

where $n(\sigma)$ is the Bose factor, $\delta^{(1)}\delta(\delta)$ the polarizability fluctuation of an isolated nanocrystal, and $F(\nu)$ is the normalized frequency distribution, which is related to the normalized inverse size distribution, $F(D^{-1})$, through equation (1) ($F(\nu)\,\mathrm{d}\nu = F(D^{\nu 1})\,\mathrm{d}D^{\nu 1}$). Obviously, $\delta^{(1)}\delta(\delta)$ is proportional to the number of atoms, N_D, in a nanocrystal when there is *intra*-nanocrystal coherence. Due to the frequency dependence of the different terms in equation (2), the scattering intensity of an assembly of nanocrystals is proportional to the frequency distribution:

$$I^{(1)}(\propto) \propto F(\propto). \tag{3}$$

Such proportionality is verified with disordered aggregates (figure 7). Let us compare the Raman spectra of amorphous aggregates and supra-crystals (figure 6(a)). The Raman peak corresponding to the supra-crystal quadrupolar modes is shifted towards a low frequency compared to the amorphous aggregate Raman peak with a decrease in its width (figure 6(b)). The narrowing of the Raman quadrupolar peak is only visible for the small supra-crystals. To explain this change in the behaviour with the ordering of nanocrystals two effects have to be taken into account.

(i) Effect of the Lorentz field. The electromagnetic field, that is induced on each nanocrystal by the (vibration-fluctuating) electric dipoles of the neighbouring nanocrystals organized in FCC supra-crystals, changes the nanocrystal polarizability fluctuation, $\alpha\alpha(\alpha)$. This effect exists if the electromagnetic fields induced by the different neighbouring nanocrystals are in phase. Consequently, electromagnetic coherence is necessary for this effect, as occurs with the supra-crystalline arrangements. In this case, the nanocrystal polarizability fluctuation,

$\alpha\alpha(\alpha)$, in a supra-crystal, is equal to the polarizability fluctuation of an isolated nanocrystal, $\delta^{(1)}\delta(\delta)$, multiplied by the factor $L(\nu)$, that accounts for the Lorentz field. $L(\nu)$ is dependent on the size D of the nanocrystals in the supra-crystal, and thus on ν through equation (1): $\delta\delta(\delta) = L(\delta)\delta^{(1)}\delta(\delta)$.

(ii) Effect of vibrational coherence.   The vibrational coherence among the nanocrystals in a supra-crystal is established due to the weak interdigitization of the thiol chains. The van der Waals bonding between thiol chains is too weak to have a measurable effect on the vibrational frequencies of nanocrystals. However, it is sufficient to establish a correlation between the vibrating nanocrystals, so that they vibrate coherently in a supra-crystal. The quadrupolar modes in a supra-crystal are like non-dispersive optical modes. For small (size $\leqslant l/10$, l being the light wavelength) supra-crystals, the light is scattered by stationary modes in the supra-crystal, as by the vibration modes in a molecule. In Raman light scattering, the vibration modes are regarded as localized, so that the momentum conservation has no need to be considered explicitly. In other words, the Raman-active modes are determined only by their symmetry. The effective supra-crystal polarizability fluctuation at the frequency n is equal to the nanocrystal polarizability fluctuation $\alpha\alpha(\alpha)$, multiplied by the number N_{SD} of nanocrystals, both in the supra-crystal. Therefore, from the above, the intensity of Raman scattering from a supra-crystal containing N_{SD} nanocrystals is proportional to $[N_{SD}L(\delta)\delta^{(1)}\delta(\delta)]^2$. Consequently, the intensity of Raman scattering from a sample organized into small supra-crystals is expressed as follows:

$$I^{(3)}(\alpha) \propto L^2(\alpha)[I^{(1)}(\alpha)]^2. \tag{4}$$

The Stokes and anti-Stokes $I^2(n)$ profiles were horizontally shifted and vertically rescaled in order to match the peak maxima. The line profile is given by the square of that corresponding to a disordered arrangement of nanocrystals. This is illustrated by figure 6(c): the narrowed peak of the 'small' supra-crystals has the same profile as the square of the non-narrowed peak of the 'disordered' aggregate. These data clearly indicate inter-nanocrystal coherence inside each highly ordered in fcc supra-crystal. Hence nanocrystals in a supra-crystal behave as atoms in a nanocrystal.

4.2. Collective optical properties

In the following we describe the optical properties of 5 nm silver nanocrystals self-organized in 2D superlattices. These properties are due to dipolar interactions induced by the close vicinity of the nanocrystals at a fixed distance from each other.

The 5 nm silver nanocrystals coated with dodecyl alkyl chains are characterized by a UV–visible absorption spectrum [61] attributed to the well-known Mie resonance centred on 2.9 eV and interband transitions at higher energy. This is in good agreement with that deduced from numerical calculations [62, 63] for particles of isolated silver spheres, taking into account the surrounding media and the presence of dodecyl alkyl chains. The influence of the chemical environment on the optical response of nanocrystals has also been demonstrated for other systems [61–65]. Various techniques such as reflectivity, laser-induced photoemission, STM and modelling have been used to demonstrate the appearance of new resonances due to the self-organization of nanocrystals in hexagonal networks. In the case of laser-induced electron photoemission, the mechanism follows a quadratic law and its yield is markedly enhanced by the surface plasmon resonance of the film made of nanocrystals organized in a compact hexagonal network. These results are in good agreement with those obtained with granular silver aggregates, produced by gas sputtering on graphite [66], and aluminium oxide [67].
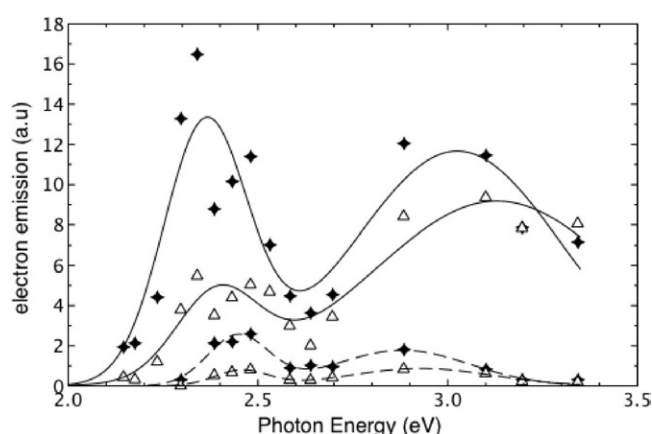
Figure 8. Photoemission spectra of the silver nanocrystal film on gold (diamonds) and HOPG (triangles) under s-polarization (dashed line) and p-polarization (solid line).

The electron photoemission spectra, measured at constant beam intensity, under s- and p-polarization, show a marked change in the electron photoemission spectrum with the light polarization (figure 8). Under p-polarization, two wide emission bands are observed, whereas under s-polarization the two peaks could be estimated as experimental errors. Under p-polarization, the electron emission intensity markedly increases with the appearance of two maxima at 2.37, 3.05 eV and 2.4 eV, 3.2 eV for gold and HOPG substrates, respectively. The increase in the electron emission yield under p-polarization is due to the optical anisotropy of the supported nanocrystal film and cannot be attributed to the intrinsic increase observed when the light is p-polarized. Hence the two electron emission peaks are related to the film made of self-organized nanocrystals, induced by hydrophobic interactions between nanocrystals. The low-energy peak is related to the longitudinal surface plasmon resonance of the film (around 2.4 eV) whereas the high-energy peak is the transverse mode. These data are in good agreement with those obtained by recording the absorption spectrum of the same nanocrystal film deposited on amorphous carbon with one peak at 2.6 eV under s-polarization and two peaks at 2.6 and 3.4 eV under p-polarization (figure 9). This is due to the fact that the electron photoemission technique is mainly related to the surface plasmon resonance absorption coefficient. These data also agree with the simulated and experimental reflectivity spectra under s- and p-polarization of the same silver nanocrystals organized in hexagonal networks [20]. These collective surface plasmon resonance modes are due to dipolar interactions between nanocrystals. This claim is also supported by photoemission induced by STM from which, by tuning the applied voltage between the tip and substrate, the electromagnetic field is at a maximum either at the top or between the nanocrystals [24]. This was also explained in terms of dipolar interactions [24, 25].

4.3. Collective magnetic properties

We know from previous studies that the hysteresis loop of nanocrystals deposited on a substrate is straighter than that obtained when the same nanocrystals are dispersed in solution [25, 28, 29]. From simulations based on the Stoner–Wohlfarth [68, 69] model and from experiments [28, 29], it has been well demonstrated that this change in the magnetic property is due to dipolar interactions. More recently it has been shown theoretically [70] that the collective magnetic properties of a film (2D) made of nanocrystals, either locally or highly
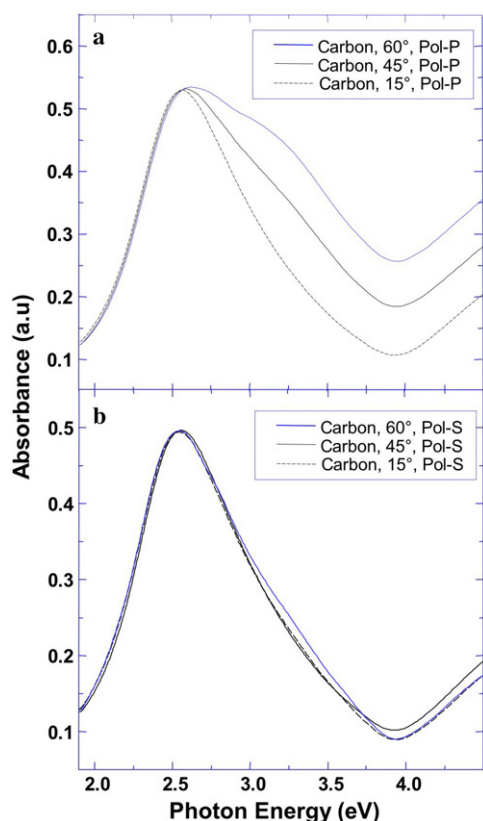
Figure 9. Absorption spectra of organized silver nanoparticles on carbon substrate. (a) Under p-polarization at different angles (15°, 45° and 60°). (b) Under s-polarization at the same angles.

ordered, do not change. This is mainly due to the fact that the magnetic properties are governed by long-range dipolar interactions. The local structure of the film is investigated in a quite general way. Two different structures are considered:

(i) A well-ordered, square-lattice monolayer, which is chosen as a reference system (figure 10(a)).
(ii) A chain-like structure of nanoparticles (figure 10(b)), considered as Stoner–Wolfarth particles, parallel to a given direction and characterized by the saturation magnetization, M_s, their anisotropy constant, K, and their diameter, D. There is no direct contact between neighbouring nanocrystals and as a result, the exchange interactions can be excluded and only dipolar interactions are taken into account.

For a perfect square lattice, with lattice spacing d, the influence of these interactions is characterized by the coupling constant, $\sigma_d = (\sigma M_s^2/12 \text{ K}) \cdot (D/d)^3$, which is the ratio of the dipolar to the anisotropy energy. To calculate σ_d^{eff} for chain-like structures, an intermediate step is first considered: a periodic arrangement of infinite parallel lines of nanocrystals at contact, parallel to the x direction of the sample. This structure is considered as a model lattice. The distance between the lines of nanocrystals of diameter D is $\sigma = (\sigma/4\sigma)D$. The total dipolar interaction energy is estimated from the sum of the dipole–dipole energies in the two opposite
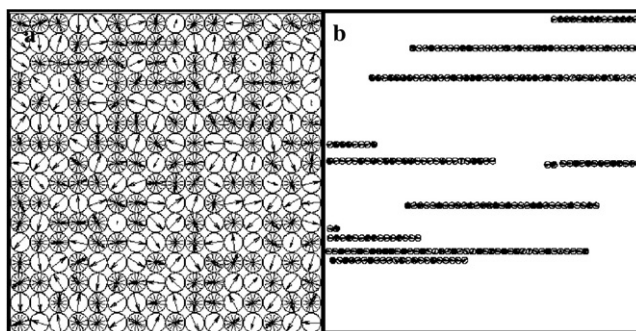
Figure 10. Configurations used in the calculation: (a) reference model, (b) linear chains. The arrows in the circles refer to the direction of the magnetic moments, which are randomly distributed.
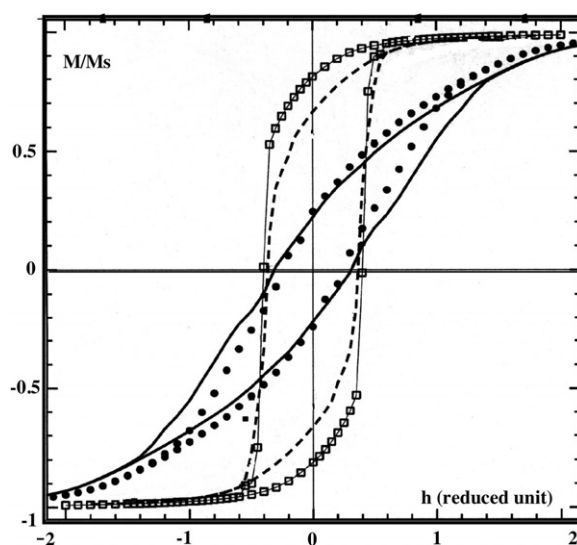

Figure 11. Hysteresis loop of the real model for linear chains. (open squares): field collinear with the chain, (circles): field perpendicular to the chain. Dotted and solid lines: corresponding perfect square model, respectively, parallel and perpendicular to the substrate. Nanocrystal diameter: 8 nm; effective coupling constant: 0.125.

cases, where all the particles have their moment oriented in the x or z direction (parallel to the chain and to the surface or normal to the chain and to the surface), respectively. The calculations are performed for both types of structures, square lattice (reference model) with an applied field parallel or normal to the surface, and chain-like (real model) with an applied field in the surface plane and parallel or perpendicular to the chains or perpendicular to the surface plane. The results of the calculations for the reference and the real system are then compared in the case of an effective coupling constant $\alpha_d^{\mathrm{eff}} = 0.125$ (figure 11). There is a marked difference between the hysteresis loop of the square lattices (dashed lines) with the effective coupling constant and that of the linear chain system (solid line) when the field is applied parallel to the chains. A large increase in the reduced remanence is obtained ($M_{\mathrm{r}}/M_{\mathrm{s}} = 0.81$) compared to the reference system ($M_{\mathrm{r}}/M_{\mathrm{s}} = 0.66$) and the coercivity slightly increases. Applying the field

Table 1. Various parameters involved in producing a well defined structure (S): size distribution (σ), deposition mode (D), van der Walls interactions (VdW), temperature (T).

S	σ	D	VdW	T
2D hexagonal network	<10%	A drop	—	Room
2D rings	All	Anticapillary Tweezer, fast evaporation	—	Room
3D supra-crystals	<10%	Control evaporation rate		20 °C < T < 30 °C
Dots	<10%	Under magnetic field	—	Room
Labyrinths	All	Under magnetic field		Room
Tubes	All	Under magnetic field	Yes	Room

perpendicular to the substrate leads to a smoother hysteresis loop, with a large decrease in the reduced remanence ($M_r/M_s = 0.20$). In this case, the coercivity slightly decreases (figure 11). Conversely to the case where the field is parallel to the chains, the hysteresis loop measured with the field perpendicular to the substrate (and accordingly also perpendicular to the chains) agrees well with that of the reference model. Indeed, due to the dipolar coupling, the linear chains behave roughly as homogeneous wires with an effective easy axis in the direction of the chains although individual nanocrystals have randomly distributed easy axes. The observed difference corresponds, to a first approximation, to the different orientations of the effective easy axes (parallel or perpendicular) of the wire with respect to the applied field. Hence, it is shown that theoretically, due to the structure, a well-ordered reference model is not relevant for calculating the hysteresis curve of linear chains. To experimentally confirm this influence of the structure of the film, the magnetic properties are determined at 3 K. In the following the applied field refers to the field used to measure the magnetization curve [71]. When the nanocrystals are oriented along a given direction and the applied field is parallel to the long axis of the chains, the hysteresis loop is squarer than that obtained for an isotropic monolayer (figure 12(a)). Note that the hysteresis loops of a perfect square lattice and isotropic disorder monolayers are the same. The magnetization properties of nanocrystals aligned in chains and 2D superlattices show an increase in the reduced remanence and coercivity whereas the saturation magnetization remains unchanged. In chain superlattices, with an applied field parallel to the substrate, the magnetic response evolves with the orientation of the applied field to the chain direction. Let us compare the magnetic properties when the applied field is perpendicular and parallel to the chain direction, keeping the substrate parallel. The magnetization is smoother than that obtained when it is parallel whereas the saturation magnetization is not reached at 2.5 T. Furthermore a drop in the reduced remanence and coercivity is observed (figure 12(b)). For a coupling constant, $\sigma_d = 0.06$, corresponding to the experimental case, the strength of the structural effect is estimated theoretically by comparing the reduced remanence either parallel or perpendicular to the chains, keeping the plane parallel to the applied field (figure 12(c)). This is compared to the experimental value (figure 12(b)) in order to check the magnitude of this structural effect on the collective magnetic properties of the cobalt nanocrystals chains. The $\sigma'_{th} = (M_r/M_s)^\sigma / (M_r/M_s)^{\sigma\sigma}$ ratios are deduced for the oriented linear chains and are found to be 0.42 from experiments and 0.77 from the model, and thus have the same order of magnitude. For this coupling strength, no change can be observed theoretically in the coercivity. This is in relatively good agreement, at a qualitative level, with the results of the model presented above. Therefore the deviation of σ' from 1 can be attributed to the modification of the structure. Our systems are not the perfect linear chains as introduced in the theoretical model. The experimental chains are larger and there are a number of bilayers in some regions of these chains. This probably explains the difference in magnitude between the experiment and the
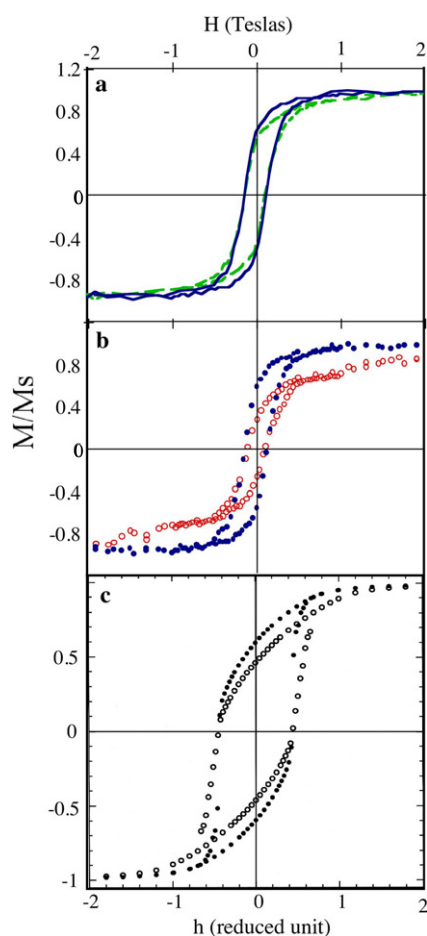
Figure 12. (a) Hysteresis curves measured at 3 K of aligned (solid lines) and partially disordered (dashed lines) 8 nm cobalt nanocrystals. The applied field is parallel to the substrate and along the direction of the particle orientation. (b) Hysteresis loop measured at 3 K when the applied field is parallel (solid circles) or perpendicular (open circles) to the nanocrystal orientation and always parallel to the substrate. (c) Calculated magnetization curves for linear chains along the x direction for $\sigma_d = 0.06$, with an applied field either parallel (solid circles) or normal (open circles) to the chain direction, keeping the substrate parallel.

theory, both for the remanence and the coercivity. The chains behave like a wire [71] with an effective easy axis in the direction of the wire.

Similar behaviour [72, 73] is observed if we compare the magnetic properties of 10 nm γFe_2O_3 nanocrystals, either self-organized in long tubes on a mesoscopic scale (inset in figure 5(c)) or forming a thin film (inset in figure 5(d)). The hysteresis loop is squarer when the field is applied parallel to the direction of the tubes (x) compared to that obtained when it is perpendicular (y). Similarly it is squarer for aligned nanocrystals compared to a rough film, (figure 13). Even though the orientation of the easy axes is energetically possible, it is demonstrated by Mossbauer spectroscopy that the easy axes of nanocrystals are mainly randomly oriented [73]. This confirms the influence of the structure of the film on the magnetic properties. However, it is possible to orient the easy axes by using cigar-shaped nanocrystals and applying a magnetic field during the deposition process [74, 75]. In this case, the hysteresis
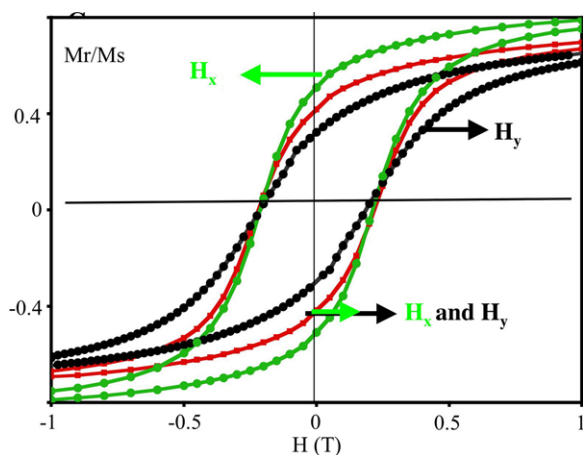
Figure 13. Magnetization curves at 3 K recorded for γFe_2O_3 nanocrystals forming tubes and recorded either parallel along (light grey (green)) or perpendicular (black) to the tube direction and forming a rough film (dark grey (red)).
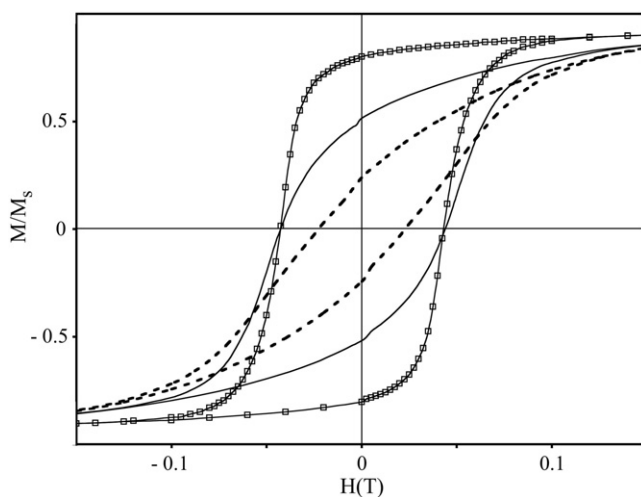
Figure 14. Magnetization curves at 290 K for cigar-shaped nanocrystals deposited on HOPG where the magnetization is recorded with an applied field either in the x direction when the nanocrystals are disordered (solid lines) and ordered (solid lines with squares) or along the y direction for ordered (dashed lines) nanocrystals.

loop is squarer when the nanocrystals are oriented along the applied field than when the nanocrystals are disordered. As above, the oriented nanocrystals behave as nanowires with a smoother hysteresis loop when the field is applied in the y direction (figure 14). These data clearly indicate that the structure of the self-assembly at a mesoscopic scale plays a role in the magnetic properties.

5. Conclusion

In this review we demonstrate that the physical properties of inorganic nanocrystals self-assembled in 2D and 3D superlattices at the mesoscopic scale markedly differ from those of

isolated nanocrystals and from the bulk phase of the material. This opens a new research area where intrinsic properties due to self-organization are observed. In the future we hope to be able to demonstrate that this is valid for a very large research domain.

References

[1] Pileni M P 2001 *J. Phys. Chem.* B **105** 3358
[2] Motte L, Billoudet F and Pileni M P 1995 *J. Phys. Chem.* **99** 16425
[3] Murray C B, Kagan C R and Bawendi M G 1995 *Science* **270** 1335
[4] Brust M, Bethell D, Schiffrin D J and Kiely C 1995 *Adv. Mater.* **9** 797
[5] Harfenist S A, Wang Z L, Alvarez M M, Vezmar I and Whetten R L 1996 *J. Phys. Chem.* **100** 13904
[6] Motte L, Billoudet F, Lacaze E and Pileni M P 1996 *Adv. Mater.* **8** 1018
[7] Whetten R L, Khoury J T, Alvarez M M, Murthy S, Vezmar I, Wang Z L, Cleveland C C, Luedtke W D and Landman U 1996 *Adv. Mater.* **8** 428
[8] Harfenist S A, Wang Z L, Alvarez M M, Vezmar I and Whetten R L 1996 *J. Phys. Chem.* **100** 13904
[9] Murthy S, Wang Z L and Whetten R L 1997 *Phil. Mag. Lett.* **75** 321
[10] Motte L, Billoudet F, Douin J, Lacaze E and Pileni M P 1997 *J. Phys. Chem.* **101** 138
[11] Motte L and Pileni M P 1998 *J. Phys. Chem.* **102** 4104
[12] Korgel B A, Fullam S, Connoly S and Fitzmaurice D 1998 *J. Phys. Chem.* **8379** 102
[13] Korgel B A and Fitzmaurice D 1999 *Phys. Rev.* B **59** 14191
[14] Courty A, Fermon C and Pileni M P 2001 *Adv. Mater.* **13** 254
[15] Courty A, Araspin O, Fermon C and Pileni M P 2001 *Langmuir* **17** 1372
[16] Lisiecki I, Albouy P A and Pileni M P 2003 *Adv. Mater.* **15** 712
[17] Lisiecki I, Albouy P A and Pileni M P 2004 *J. Phys. Chem.* B **108** 20050
[18] Brust M 2005 *Nat. Mater.* **4** 354
[19] Pileni M P (ed) 2005 *Nanocrystals Forming Mesoscopic Structures* (New York: Wiley)
[20] Taleb A, Petit C, Pileni M P and Pileni M P 1998 *J. Phys. Chem.* B **102** 2214
[21] Taleb A, Russier V, Courty A and Pileni M P 1999 *Phys. Rev.* B **59** 13350
[22] Pinna N, Maillard M, Courty A, Russier V and Pileni M P 2002 *Phys. Rev.* B **66** 45415
[23] Maillard M, Monchicourt P and Pileni M P 2003 *Chem. Phys. Lett.* **107** 7492
[24] Nilius N, Benia H N, Salzemann C, Freund H J, Brioude A and Pileni M P 2005 *Chem. Phys. Lett.* **413** 10
[25] Silly F, Gusev A O, Taleb A, Charra F and Pileni M P 2000 *Phys. Rev. Lett.* **84** 5840
[26] Silly F, Gusev A O, Taleb A, Pileni M P and Charra F 2001 *Appl. Phys. Lett.* **79** 263
[27] Petit C, Taleb A and Pileni M P 1998 *Adv. Mater.* **10** 259
[28] Sun C B, Murray, Weller D, Folks L and Moser A 2000 *Science* **287** 1989
[29] Petit C, Taleb A and Pileni M P 1999 *J. Phys. Chem.* B **103** 1805
[30] Russier V, Petit C, Legrand J and Pileni M P 2000 *Phys. Rev.* B **62** 3910
[31] Russier V, Petit C and Pileni M P 2003 *J. Appl. Phys.* **93** 10001
[32] Markovich G, Collier C P and Heath J R 1998 *Phys. Rev. Lett.* **80** 3807
[33] Taleb A, Silly F, Gussev A O, Charra F and Pileni M P 2000 *Adv. Mater.* **12** 633
[34] Germain V and Pileni M P 2005 *Adv. Mater.* **17** 1424
[35] Germain V and Pileni M P 2005 *J. Phys. Chem.* **109** 5548
[36] Courty A, Merme A, Albouy P A, Duval E and Pileni M P 2005 *Nat. Mater.* **4** 395
[37] Duval E, Merme A, Courty A, Albouy P A and Pileni M P 2005 *Phys. Rev.* B **72** 85439
[38] Courty A, Merme A, Albouy P A, Duval E and Pileni M P 2005 *J. Phys. Chem.* **109** 21159
[39] Pileni M P (ed) 1989 *Reverse Micelles* (Amsterdam: Elsevier)
[40] Motte L, Lisiecki I and Pileni M P 1994 *Hydrogen Bond Networks* ed J Dore and M C Bellisan (Dordrecht: Kluwer Academic) p 447
[41] Pileni M P, Hickel B, Ferradini C and Pucheault J 1982 *Chem. Phys. Lett.* **92** 308
[42] Pileni M P 1993 *J. Phys. Chem.* **97** 6961
[43] Petit C and Pileni M P 1988 *J. Phys. Chem.* **92** 2282
[44] Petit C, Lixon P and Pileni M P 1990 *J. Phys. Chem.* **94** 1598
[45] Kirkland A, Jefferson D A, Duff D G, Edwards P P, Gameson I, Johnson B F G and Smith D J 1993 *Proc. R. Soc.* A **440** 589
[46] Lisiecki I and Pileni M P 1993 *J. Am. Chem. Soc.* **115** 3887
[47] Salzemann C, Lisiecki I, Urban J and Pileni M P 2004 *Langmuir* **20** 11772
[48] Urban J 1998 *Cryst. Res. Technol.* **33** 7

[49] Courty A, Lisiecki I and Pileni M P 2002 *J. Chem. Phys.* **116** 8074
[50] Jiang X C, Brioude A and Pileni M P 2006 *Colloids Surf.* A **277** 201
[51] Germain V, Richardi J, Ingert D and Pileni M P 2005 *J. Phys. Chem.* B **109** 5541
[52] Lalatonne Y, Richardi J and Pileni M P 2004 *Nat. Mater.* **3** 121
[53] Latonne Y, Motte L, Richardi J and Pileni M P 2005 *Phys. Rev.* E **71** 11404
[54] Palpant B, Portales H, Saviot L, Lermé J, Prével B, Pellarin M, Duval E, Perez A and Broyer M 1999 *Phys. Rev.* B **60** 17107
[55] Duval E, Boukenter A and Champagnon B 1986 *Phys. Rev. Lett.* **56** 2052
[56] Lamb H 1882 *Proc. Lond. Math. Soc* **13** 189
[57] Duval E 1992 *Phys. Rev.* B **46** 5795
[58] Fuiji M, Nagareda T, Hayashi S and Yamamoto K 1991 *Phys. Rev.* B **44** 6243
[59] Portales H, Saviot L, Duval E, Fujii M, Hayashi S, Del Fatti N and Vallée F 2001 *J. Chem. Phys.* **115** 3444
[60] Duval E, Portales H, Saviot L, Fujii M, Sumitomo K and Hayashi S 2001 *Phys. Rev.* B **63** 075405
[61] Taleb A, Petit C and Pileni M P 1998 *J. Phys. Chem.* B **102** 2214
[62] Toennies J P 1993 *Optical Properties of Metal Clusters* (*Springer Series in Material Science* vol 25) ed U Kreibig and M Vollmer (Berlin: Springer)
[63] Persson B N J 1993 *Surf. Sci.* **281** 153
[64] Mulvaney P 1996 *Langmuir* **12** 788
[65] Malinsky M D, Kelly K L, Schatz G C and Van Duyne R P 2001 *J. Am. Chem. Soc.* **123** 1471
[66] Lehmann J, Merschdorf M, Pfeiffer W, Thon A, Voll S and Gerber G 2000 *J. Chem. Phys.* **112** 5428
[67] Monchicourt P, Raynaud M, Saringar H and Kupersztych J 1997 *J. Phys.: Condens. Matter* **9** 5765–75
[68] Stoner E C and Wohlfarth E P 1948 *Phil. Trans. R. Soc.* A **240** 599
Stoner E C and Wohlfarth E P 1991 *IEEE Trans. Magn.* **27** 3475 (reprint)
[69] Pfeiffer H 1990 *Phys. Status Solidi* a **122** 377
[70] Russier V, Petit C, Legrand J and Pileni M P 2000 *Appl. Surf. Sci.* **164** 186
[71] Encinas-Oropesa A, Demand M, Pinaux L, Ebels U and Huynen I 2001 *J. Appl. Phys.* **89** 6704
[72] Ngo A T and Pileni M P 2000 *Adv. Mater.* **12** 276
[73] Lalatonne Y, Motte L, Russier V, Ngo A T, Bonville P and Pileni M P 2004 *J. Phys. Chem.* B **12** 276
[74] Ngo A T and Pileni M P 2002 *J. Appl. Phys.* **92** 4649
[75] Ngo A T and Pileni M P 2003 *Colloids Surf.* A **228** 107